Experimental and theoretical models of wave-induced flexure of a sea ice floe

M. H. Meylan[1], L. G. Bennetts[2], C. Cavaliere[3], A. Alberello[4] and A. Toffoli[4]

[1]School of Mathematical and Physical Sciences, University of Newcastle, Callaghan 2308, Australia

[2]School of Mathematical Sciences, University of Adelaide, Adelaide 5005, Australia

[3]Polytechnic University of Milan, Milan 20133, Italy

[4]Centre for Ocean Engineering Science and Technology, Swinburne University of Technology, Melbourne 3122, Australia

April 30, 2015

Abstract

An experimental model is used to validate a theoretical model of a sea ice floe's flexural motion, induced by ocean waves. A thin plastic plate models the ice floe in the experiments. Rigid and compliant plastics and two different thicknesses are tested. Regular incident waves are used, with wavelengths less than, equal to and greater than the floe length, and steepnesses ranging from gently sloping to storm-like. Results show the models agree well, despite the overwash phenomenon occurring in the experiments, which the theoretical model neglects.

Large-amplitude ocean surface waves are now a prominent feature in regions of the Arctic Ocean partially covered by sea ice (Francis et al., 2011; Khon et al., 2014; Thomson and Rogers, 2014). Climate change has weakened and fragmented the ice cover to the extent that open ocean swells travel deep into the ice-covered ocean and fetch is generated in open water between interspersed ice floes.

Waves cause ice floes to bend and flex. The flexural motion imposes strains on the floes (Langhorne et al., 1998). If the strains are sufficiently large the floes break-up into smaller floes (Prinsenberg and Peterson, 2011), which are more susceptible to melting (Steele, 1992). Waves also introduce warm water and wash over the floe surfaces, further increasing melt rates (Wadhams et al., 1979; Massom and Stammerjohn, 2010). Thus, waves augment warmer temperatures in driving the retreat of Arctic sea ice (Squire, 2011).

In the Antarctic, Southern Ocean storm waves penetrate deep into the ice-covered ocean. Kohout et al. (2014) used in-situ measurements of waves to show that large-amplitude storm waves maintain sufficient energy to break-up floes over 400 km into the ice-covered ocean. Further, they used numerical models and satellite data to identify a negative correlation between trends in local wave activity and trends in regional ice extent.

Wave-ice interactions are now being integrated into large-scale models used for operational wave/ice forecasting and climate studies (e.g. Doble and Bidlot, 2013; Williams et al., 2013a,b). The interactions are parameterised in the large-scale models using predictions given by theoretical models. Williams et al. (2013a), for example, parameterise floe break-up using a theoretical model of the wave-induced flexural motion of a floe.

The theoretical models use potential flow theory to model the water and thin-plate theory to model the ice floes. The models have been developed over 40 years, as documented in the reviews of Squire et al. (1995) and Squire (2007). They typically model the flexural response of the floes to waves, i.e. vertical displacements. Lateral motions, such as surge and drift, are neglected.

Moreover, existing models are based on linear theory. Thus, they do not account for the highly nonlinear phenomena inherent in wave-floe interactions. In particular, waves of modest amplitude wash over the floes due to their small freeboards. Overwash violates the assumptions undergirding the
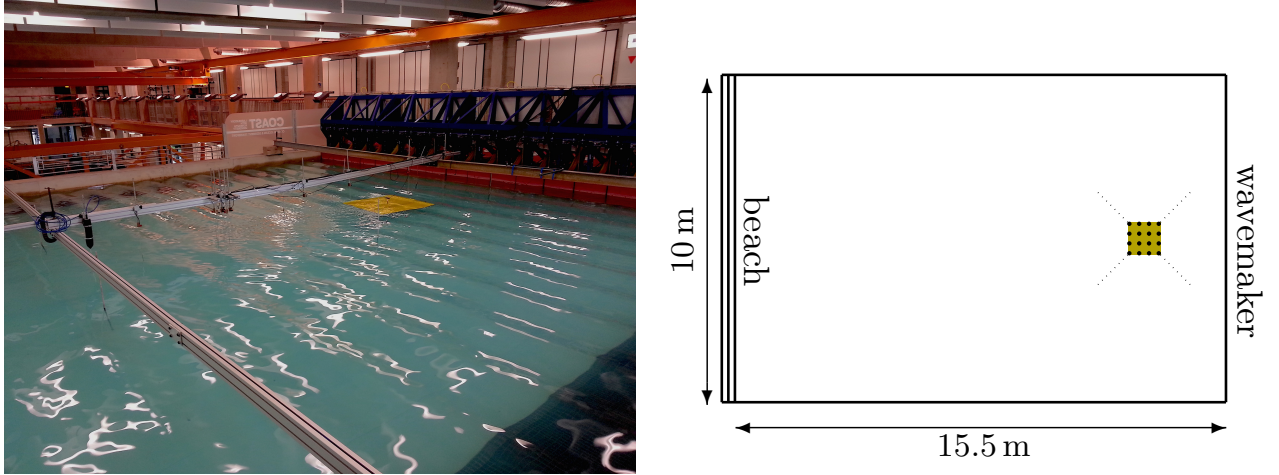
Figure 1: Experimental set-up. Left-hand panel: photo of wave basin and model floe. (Note, a gold surface was used to help highlight the floe in the photo). Right: schematic plan view of basin, including model floe (gold square), markers (black dots) and mooring lines (dotted lines).

linear theory of wave-floe interactions, i.e. all motions are small perturbations from the equilibrium. Further, overwash applies a moving and uneven load to the floe surface.

Montiel et al. (2013b,a) conducted a series of laboratory wave basin experiments to validate the linear theoretical model of wave interactions with an ice floe. In keeping with the theoretical models, they used a thin (plastic) plate to model the ice floe. Tests were conducted for regular incident waves, using a range of wave periods and two very mild steepnesses, 0.01 and 0.02.

Notably, Montiel et al. (2013b,a) applied constraints to the model floe to match the assumptions of the theoretical models. They suspended a vertical rod through a small hole in the center of the floe to eliminate surge and drift. They also added a barrier around the edge of the floe to prevent overwash. Subsequently, the experiment-theory agreement they found does not necessarily imply the theoretical model will predict the floe's wave-induced flexural motion accurately, in the more realistic setting when overwash and lateral motions are permitted.

A new and independent experimental campaign was conducted in the wave basin facility at the Coastal Ocean and Sediment Transport (COAST) laboratories of Plymouth University, U.K. The wave basin is $10\,\mathrm{m}$ wide and $15.5\,\mathrm{m}$ long. The basin was filled with fresh water of density $\rho \approx 1000\,\mathrm{kg\,m^{-3}}$ and $H = 0.5\,\mathrm{m}$ deep. Figure 1 shows a photo of the facility and a plan view of the experimental set-up.

A model ice floe was installed in the basin. Following previous experimental and theoretical models referenced above, a thin plastic plate was used to model the floe. However, unlike the experimental model of Montiel et al. (2013b,a), a barrier was not attached to the edge of the floe, and the floe was only loosely moored. Waves were, therefore, capable of overwashing the floe, and the floe could surge back and forth and drift to a certain extent. The electronic supplementary material (ESM) contains a typical example of the lateral motions (surge and drift). It shows the long-period motion ($> 20\,\mathrm{s}$) induced by the mooring system does not affect the short-period surge motion. The lateral motions are not analysed further in this investigation.

Two different types of plastic, with distinct material properties, were used. First, a relatively dense and rigid polypropylene plastic, with a manufacturer specified density of $\rho_{\mathrm{pl}} = 905\,\mathrm{kg\,m^{-3}}$ and Young's modulus $E = 1600\,\mathrm{MPa}$. Second, a relatively light and compliant polyvinyl chloride (PVC) plastic with density $\rho_{\mathrm{pl}} = 500\,\mathrm{kg\,m^{-3}}$ and Young's modulus $E = 500\,\mathrm{MPa}$. Both plastics were provided with thicknesses $h = 5\,\mathrm{mm}$ and $10\,\mathrm{mm}$. The plates were cut into squares with side lengths $2L = 1\,\mathrm{m}$.

A series of tests were conducted in which the model floes were set in motion by regular incident
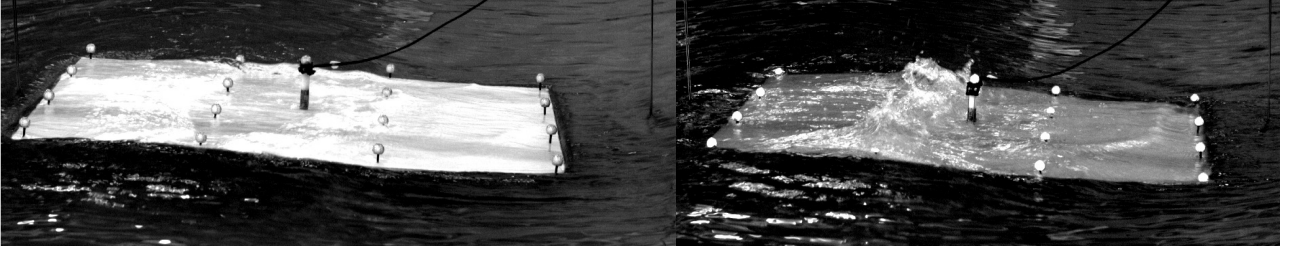
Figure 2: Photographs of mild (left-hand panel) and severe (right) overwash.

waves. The motions were recorded stereoscopically by the Qualysis motion tracking system, which comprises infrared cameras, sixteen 30 mm diameter spherical markers and software. The markers were attached to the floe surfaces in a square lattice. The Qualysis system provides the three-dimensional locations of the markers at a 200 Hz frequency.

A wave maker, installed at the right-hand end of the basin, was used to generate the incident waves. A beach was located at the left-hand end of the basin to absorb a proportion of the wave energy reaching it. The wave maker consists of twenty active pistons, which further absorbed wave energy reflected back to it. Preliminary tests, conducted without the model floe, showed reflected waves contributed less than 1% of wave energy in the basin center. The theoretical model outlined below, therefore, neglects reflected wave fields.

Wave periods $T = 0.6$ s, 0.8 s and 1 s were used for the incident waves. Four incident wave steepnesses were tested, ranging from mild and gently sloping to energetic and storm-like. The steepnesses were $ka = 0.04$, 0.08, 0.1 and 0.15, where k denotes the incident wave number, i.e. the positive real root of the dispersion relation

$$k \tanh(kH) = \frac{\omega^2}{g} \qquad \text{where} \qquad \omega = \frac{2\pi}{T} \tag{1}$$

and $g \approx 9.81 \, \mathrm{m\,s^{-2}}$ is acceleration due to gravity, and a denotes the incident amplitude. The wavelengths corresponding to the periods 0.6 s, 0.8 s and 1 s are $\lambda = 2\pi/k = 0.56$ m, 1.00 m and 1.51 m, respectively, i.e. approximately half the floe length, equal to the floe length and 1.5 times the floe length. (Due to time constraints, not all steepness, period, thickness, plastic combinations were tested.)

The incident waves overwashed the model floes in approximately 60% of the cases tested. The polypropylene floes, which have a relatively small freeboard, experienced the strongest overwash. The overwashed fluid, measured by a small wave gauge at the center of the floe, was up to 3.5 mm deep, which occurred for a 5 mm thick polypropylene floe and an incident wave of length 1.00 m and amplitude 24 mm (steepness 0.15). The depth represents the mean over test duration. Incident wave amplitudes were approximately an order of magnitude greater than the corresponding overwash depths.

Figure 2 shows two photos of overwash occurring in the tests. The left-hand panel shows an example of mild overwash occurring for a 10 mm thick PVC floe and an incident wave with length 1.51 m and steepness 0.15. A bore wave is visible in the shallow overwash. Bores are typical when overwash occurs. The right-hand panel shows an example of severe overwash occurring for a 10 mm thick polypropylene floe and an incident wave with length 1.51 m and steepness 0.15. The second deepest overwash of 2.8 mm occurred in this test and the incident amplitude was 37 mm. In the instant captured, bore waves travelling up and down the plate have collided and, subsequently, caused breaking. The ESM provides high-definition movies corresponding to the photos.

The most energetic waves also slammed the floe edges against the water surface, i.e. the edges of the floe briefly lost contact with the water surface. Slamming was visibly strongest for the denser

polypropylene floes.

For each test conducted, the recorded flexural motions of the floe are converted into a spectral representation via a decomposition into the floe's natural modes of vertical vibration *in vacuo*. The modes are denoted $w_j(\mathbf{x})$ ($j = 1, 2, \dots$), where the Cartesian coordinate $\mathbf{x} = (x, y)$ defines horizontal locations on the surface of the floe. The origin of the coordinate system is the geometric center of the floe. The x coordinate points in the direction of the incident wave. Following Kirchoff-Love thin-plate theory (Timoshenko and Woinowsky-Krieger, 1959), the modes satisfy the governing equation

$$\Delta^2 w_j = \mu_j^4 w_j \qquad \text{for} \quad \mathbf{x} \in \Omega = \{x, y : -L < x, y < L\}, \tag{2}$$

where μ_j are eigenvalues, plus free-edge conditions. The modes, therefore, depend on the shape of the floe only. The modes are orthonormal, i.e.

$$\iint_\Omega w_i(\mathbf{x}) w_j(\mathbf{x}) \, \mathrm{d}\mathbf{x} = \delta_{ij}, \tag{3}$$

where δ_{ij} is the Kronecker delta. They are calculated using the finite element method outlined by Meylan (2002).

Let $\eta_m(t)$ denote the vertical displacement of the mth marker. After the initial transients have passed, the signal is approximately harmonic in time at the angular frequency of the incident wave, ω. Therefore, a complex amplitude A_m is calculated such that $\eta_m(t) \approx \mathrm{Re}\{A_m \mathrm{e}^{-\mathrm{i}\omega t}\}$, using least-squares minimization.

The complex amplitudes A_m are projected onto a finite-dimensional space spanned by the dominant natural modes of vibration, i.e.

$$A_m \approx \sum_{j \in \Lambda} \xi_j^{\mathrm{ex}} w_j(\mathbf{x}_m) \qquad \text{for} \quad m = 1, \dots, 16, \tag{4}$$

where $\mathbf{x}_m$ denotes the location of the mth marker. The set Λ contains indices of the modes used for computations. The number of flexural modes excited depends on the relative properties of the incident wave and the floe. Higher-order flexural modes are excited as the incident wavelength to floe length ratio becomes smaller, i.e. kL decreases. Here $\Lambda = \{1, 2, 5, 6, 7, 9, 11\}$ is set for all tests. The set contains only vertical motions symmetric with respect to the direction of the incident wave are considered. The first two modes represent the rigid body motions of the floe: heave and pitch, respectively. The final five modes represent the primary flexural motions. The weights ξ_j^{ex} are obtained via a least squares minimization routine. The method is robust with respect to occasional instances of signal loss, when severe overwash submerged the markers.

Figure 3 shows an example decomposition of the floe motion into the natural modes. This is for a 5 mm thick PVC floe, and an incident wave with length 1.00 m and steepness 0.1. The left-hand panel shows the recorded vertical displacements of the markers over a short time interval. The right-hand panels show the corresponding four dominant weighted flexural modes.

The complementary theoretical model used is based on linear potential flow theory for the water motions and Kirchoff-Love thin-plate theory for the floe motions, which is standard for modelling wave-floe interactions (Squire et al., 1995; Squire, 2007). The solution method employed for the three-dimensional water domain and square floes is almost identical to that developed by Meylan (2002).

Potential flow theory assumes the water is homogeneous, inviscid, incompressible and in irrotational motion. Linear theory assumes the incident wave steepness is small, i.e. $ka \ll 1$, and all motions are small perturbations from the equilibrium. Thin-plate theory assumes the floe's flexural motions can be obtained from the vertical displacements of its lower surface.

Locations in the water are defined by the Cartesian coordinate system (x, y, z), where $\mathbf{x} = (x, y)$ defines horizontal locations and z is the vertical coordinate. The water extends to infinity in all horizontal directions. Where the floe covers the water surface, the horizontal coordinate coincides
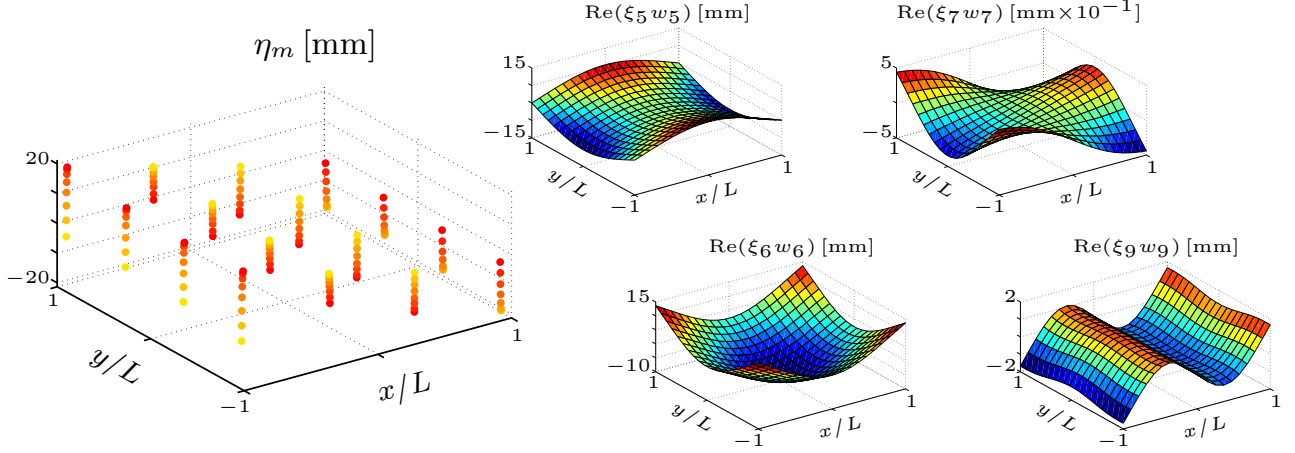
4

Figure 3: Example decomposition of recorded floe motion into natural modes of vibration. Left-hand panel: motion of floe markers every $0.03\,$s over a $0.21\,$s interval (yellow to red in increasing time). Right panels: corresponding four dominant flexural modes.

with the horizontal coordinate system defined for the floe. The vertical coordinate points upwards and its origin is set to coincide with the water surface in equilibrium.

Following linear potential flow theory and assuming time-harmonic conditions, the water's velocity field is defined by the gradient of the scalar velocity potential $\mathrm{Re}\,\{\phi(x,y,z)\mathrm{e}^{-\mathrm{i}\omega t}\}$. The time-independent component of the velocity potential, ϕ, satisfies Laplace's equation throughout the water domain, i.e.

$$\Delta\phi = 0 \quad \text{for} \quad \mathbf{x} \in \mathbb{R}^2 \quad \text{and} \quad -H < z < 0, \tag{5a}$$

and a zero normal flow bed condition

$$\phi_z = 0 \quad \text{for} \quad \mathbf{x} \in \mathbb{R}^2 \quad \text{and} \quad z = -H. \tag{5b}$$

On the linearised water surface away from the floe, the velocity potential satisfies the free-surface condition

$$\phi_z = \frac{\omega^2}{g}\phi \quad \text{for} \quad \mathbf{x} \notin \Omega \quad \text{and} \quad z = 0. \tag{5c}$$

On the linearised interface between the water surface and the underside of the floe, the velocity potential is coupled to the floe motion via kinematic and dynamic conditions, respectively

$$\partial_z\phi = -\mathrm{i}\omega\sum_{j=1}^{\infty}\xi_j^{\text{th}}w_j, \tag{5d}$$

$$\text{and} \quad \frac{\mathrm{i}\omega}{g}\phi = \sum_{j=1}^{\infty}\left(1 + \beta\mu_j^4\right)\xi_j^{\text{th}}w_j - \omega^2\gamma\sum_{j=1}^{\infty}\xi_j^{\text{th}}w_j, \tag{5e}$$

both for $\mathbf{x} \in \Omega$ and $z = 0$. Here, $\gamma = \rho_{\mathrm{pl}}h/\rho g$ is the scaled mass of the floe and $\beta = Eh^3/\{12(1-\nu^2)\rho g\}$ is the scaled flexural rigidity, where $\nu = 0.4$ (polypropylene floes) and 0.3 (PVC) are typical values of Poisson's ratio. Following Montiel et al. (2013b,a), who measured the Young's moduli of their PVC floes to be approximately $250\,$MPa less than the manufacturer specified values, a reduced Young's modulus of $E = 500\,$MPa is used in the model to represent the PVC floes.

The modal weights, ξ_j^{th}, must be obtained as part of the solution process. The coupling equations (5d–e) assume the shallow-draught approximation and that the underside of the floe is in contact with

the water surface at all points and at all times during the motion. Sommerfeld radiation conditions are also applied to the velocity potential.

Using linearity, the velocity potential is expanded as

$$\phi = \phi^{\mathrm{I}} + \phi^{\mathrm{D}} - \mathrm{i}\omega \sum_{j=1}^{\infty} \xi_j^{\mathrm{th}} \phi_j^{\mathrm{R}} \quad \text{where} \quad \phi^{\mathrm{I}} = \frac{ga\mathrm{e}^{\mathrm{i}kx}\cosh\{k(z+H)\}}{\mathrm{i}\omega\cosh kH} \tag{6}$$

is the incident wave potential (Bishop et al., 1986; Newman, 1994). The sum of the incident wave and diffraction potentials, $\phi^{\mathrm{I}} + \phi^{\mathrm{D}}$, is the solution of the problem in which the floe is held in place, i.e. equations (5a–d) with $\xi_j^{\mathrm{th}} = 0$ $(j = 1, 2, \dots)$. The radiation potentials, ϕ_j^{R} $(j = 1, 2, \dots)$ are solutions of the problems in which the floe oscillates in one of its degrees of freedom with unit amplitude, i.e. equations (5a–d) with $\xi_i^{\mathrm{th}} = \delta_{ij}$ $(i = 1, 2, \dots)$.

On the linearised water surface, $z = 0$, the diffraction and radiation potentials can be expressed as

$$\phi^{\mathrm{D}}(\mathbf{x}, 0) = \frac{\omega^2}{g} \iint_{\Omega} G(\mathbf{x}, 0 : \mathbf{x}') \left(\phi^{\mathrm{I}}(\mathbf{x}', 0) + \phi^{\mathrm{D}}(\mathbf{x}', 0) \right) \, \mathrm{d}\mathbf{x}', \tag{7a}$$

$$\text{and} \quad \phi_j^{\mathrm{R}}(\mathbf{x}, 0) = \iint_{\Omega} G(\mathbf{x}, 0 : \mathbf{x}') \left(\frac{\omega^2}{g} \phi_j^{\mathrm{R}}(\mathbf{x}', 0) - w_j(\mathbf{x}') \right) \, \mathrm{d}\mathbf{x}' \quad \text{for} \quad j = 1, 2 \dots. \tag{7b}$$

Here $G(\mathbf{x}, z : \mathbf{x}')$ is the Green's function, which satisfies the governing equations for a free-surface flow and is forced at the point $\mathbf{x}'$ on the surface, i.e.

$$\Delta G = 0 \quad \text{for} \quad \mathbf{x} \in \mathbb{R}^2 \quad \text{and} \quad -H < z < 0, \tag{8a}$$

$$\partial_z G = 0 \quad \text{for} \quad \mathbf{x} \in \mathbb{R}^2 \quad \text{and} \quad z = -H, \tag{8b}$$

$$\partial_z G - \frac{\omega^2}{g} G = \delta(\mathbf{x} - \mathbf{x}') \quad \text{for} \quad \mathbf{x} \in \mathbb{R}^2 \quad \text{and} \quad z = 0, \tag{8c}$$

and the Sommerfeld radiation condition that the waves are outgoing as $|\mathbf{x}| \to \infty$. Expressions (7a–b) are solved for $\mathbf{x} \in \Omega$ using a constant panel method (see Meylan, 2002).

A linear system for the modal weights, ξ_j^{th}, is obtained by applying the dynamic coupling condition (5e) to the expanded velocity potential (6) and taking inner-products with respect to the subset of the modes defined by Λ. The system is expressed in matrix form as

$$\left(\mathbf{K} + \mathbf{C} - \omega^2 \mathbf{M} - \omega^2 \mathbf{A}(\omega) - \mathrm{i}\omega \mathbf{B}(\omega) \right) \boldsymbol{\xi}^{\mathrm{th}} = \mathbf{f}(\omega). \tag{9}$$

Here $\mathbf{K}$, $\mathbf{C}$ and $\mathbf{M}$ are stiffness, hydrostatic-restoring and mass matrices, respectively, and are defined by

$$\mathbf{K} = \lceil \beta \mu_j^4 \rceil, \qquad \mathbf{C} = \mathbf{I}, \qquad \text{and} \qquad \mathbf{M} = \gamma \mathbf{I}, \tag{10}$$

where $\lceil \dots \rceil$ denotes a diagonal matrix and $\mathbf{I}$ is the identity matrix. The real matrices $\mathbf{A}$ and $\mathbf{B}$ are known as the added-mass and damping matrices, respectively, and are defined element-wise by

$$\omega^2 \mathbf{A}_{ij} + \mathrm{i}\omega \mathbf{B}_{ij} = \frac{\omega^2}{g} \iint_{\Omega} \phi_j^{\mathrm{R}}(\mathbf{x}, 0) w_i(\mathbf{x}) \, \mathrm{d}\mathbf{x}. \tag{11}$$

The forcing vector, $\mathbf{f}$, is defined by

$$\mathbf{f}_j = \frac{\mathrm{i}\omega}{g} \iint_{\Omega} \left(\phi^{\mathrm{I}}(\mathbf{x}, 0) + \phi^{\mathrm{D}}(\mathbf{x}, 0) \right) w_j(\mathbf{x}) \, \mathrm{d}\mathbf{x}. \tag{12}$$
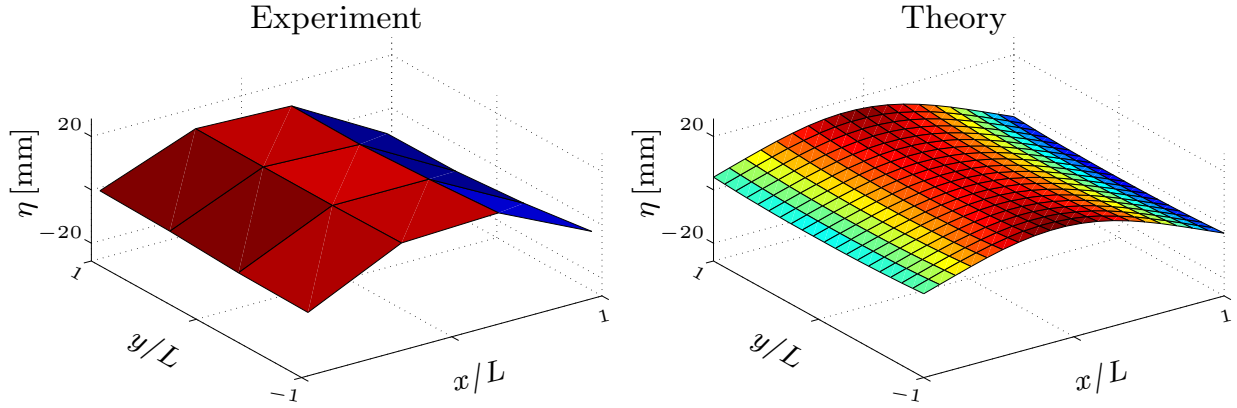
Figure 4: Example comparison of floe motion at an instant in time recorded during a test (left-hand panel) and predicted by theoretical model (right), for a 5 mm thick PVC floe and an incident wave with length 1.51 m and steepness 0.08.

The system is solved for the modal weights, which are contained in the vector $\boldsymbol{\xi}^{\mathrm{th}}$, thus completing the solution process. The ESM provides model predictions of the modal weights as functions of wave period, which show the dominant modes experience few resonances over the period range considered.

Figure 4 shows an example comparison of a floe's flexural motion at an instant, as measured during an experiment and as predicted by the theoretical model. The instant is during the time-harmonic phase of the floe's motion in the experiment. The example is for a 5 mm thick PVC floe and an incident wave with length 1.51 m and steepness 0.08. The motions were synchronised by multiplying the theoretical model predictions by the (almost) constant phase difference between it and the experimental motions following the transient stage. The snapshot is indicative of the pleasing agreement found between the model and experimental data. Example animations of the experiment-theory comparisons are provided in the ESM.

Figures 6–5 quantify the experiment-theory agreement in terms of the magnitudes of the dominant modes. Figure 6 shows results for the PVC floes and figure 5 shows results for the polypropylene floes. The magnitudes of the modal weights are scaled with respect to the incident amplitude, a. Results for mode 11 are omitted for presentational purposes, but can be found in the ESM.

The experimental data indicate the floe's motion is, essentially, linear, i.e. the modal weights scale with the incident amplitude. Small discrepancies are notable for certain cases, for example, the 1.51 m long, 0.08 steep incident waves for a 10 mm thick PVC floe. However, no consistent dependence is evident in those cases, and experimental errors are a probable cause of the discrepancies, which could be caused by the tracking system accuracy or aliasing in the modal decomposition. The relatively large scatter of the experimental data for the incident waves with length 0.56 m and polypropylene floes is attributed to slow irregular rotational yaw motions, as shown by the asymmetries visible in the final example provided in the ESM. These are caused by second order effects and interactions with the mooring.

The model is able to capture the magnitudes of the modal weights accurately. The model predictions are marginally more accurate for the thinner floes. Note that the logarithmic scale used to display the results emphasises errors for modal weights with small magnitudes.

The experiment-theory agreement found indicates that nonlinear phenomena inherent in wave-floe interactions, in particular, overwash, but also slamming, drift and (linear) surge, have only a negligible affect on the floe's flexural motions. The agreement holds for: a relatively dense and rigid floe and a relatively light and compliant floe; incident wavelengths less than, equal to and greater than the floe
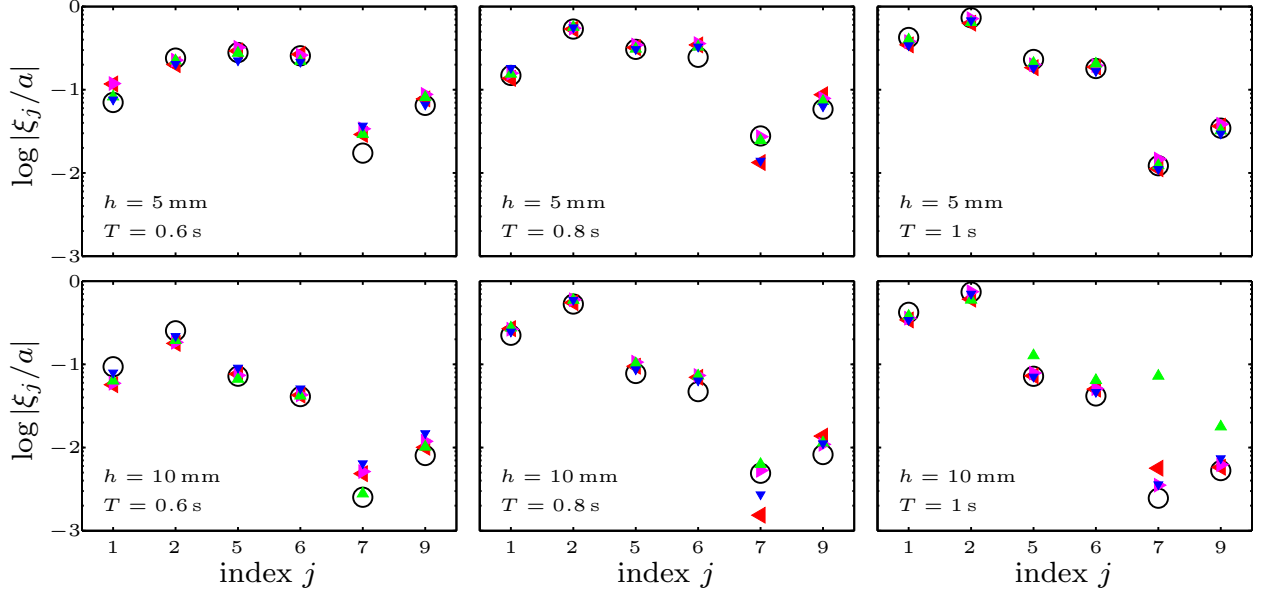
Figure 5: Comparison of scaled modal weight magnitudes extracted from experimental data (triangles) and predicted by theoretical model for PVC floes (black circles), plotted on a log scale. Incident steepnesses are: $ka = 0.04$ (blue, triangles down); 0.08 (green, up); 0.1 (magenta, right); and 0.15 (red, left).
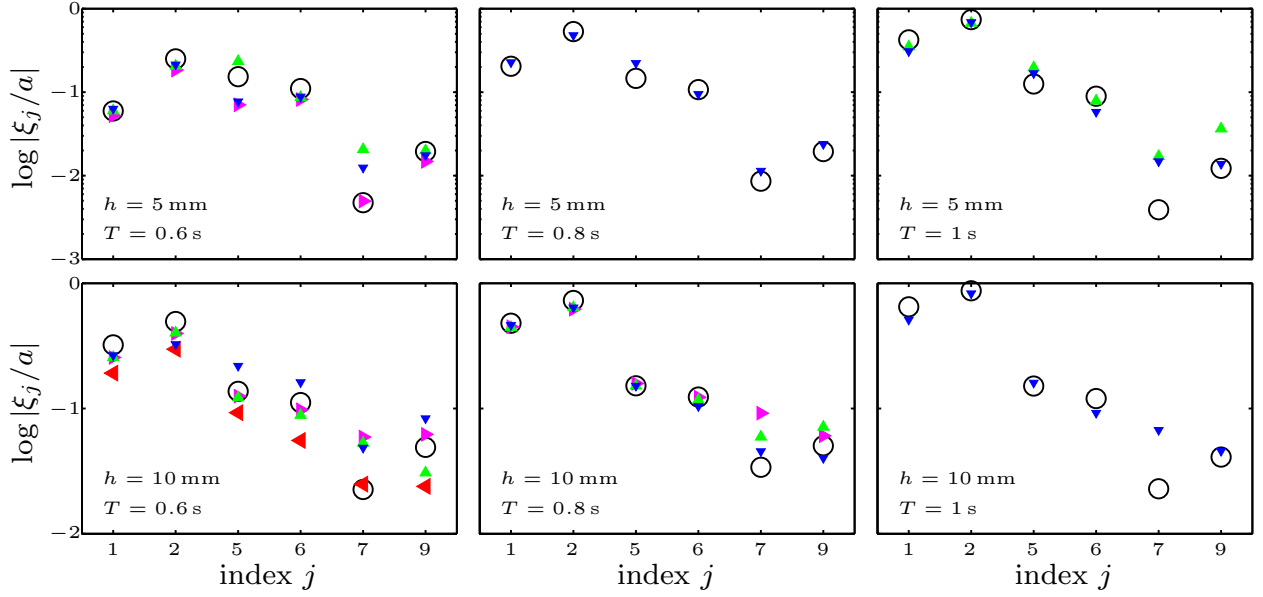

Figure 6: As in figure 6 but for polypropylene floes.

length; and mild, gently-sloping to energetic, storm-like incident waves.

In conclusion, relatively simple models of wave-ice interactions, based on linear potential flow and thin-plate theories, are viable to model motions of sea ice floes induced by ocean surface waves. The assumption that an ice floe can be modelled as a floating, thin plate has not yet been tested directly. It is likely that its validity will depend on the ice type, as dictated by the prevailing season and geographic location.

Acknowledgments

References

R. E. D. Bishop, W. G. Price, and Y. Wu. A general linear hydroelasticity theory of floating structures moving in a seaway. *Phil. Trans. R. Soc. Lond. A*, 316(1538):375–426, 1986.

M. J. Doble and J.-R. Bidlot. Wavebuoy measurements at the Antarctic sea ice edge compared with an enhanced ECMWF WAM: progress towards global waves-in-ice modeling. *Ocean Model.*, 70:166–173, 2013.

O. P Francis, G. G. Panteleev, and D. E. Atkinson. Ocean wave conditions in the Chukchi sea from satellite and in situ observations. *Geophys. Res. Lett.*, 38:L24610, 2011.

V. C. Khon, I. I. Mokhov, F. A. Pogarskiy, A. Babanin, K. Dethloff, A. Rinke, and H. Matthes. Wave heights in the 21st century Arctic Ocean simulated with a regional climate model. *Geophys. Res. Lett.*, 41:2956–2961, 2014.

A. L. Kohout, M. J. M. Williams, S. M. Dean, and M. H. Meylan. Storm-induced sea ice breakup and the implications for ice extent. *Nature*, pages 604–607, 2014.

P. J. Langhorne, V. A. Squire, C. Fox, and T. G. Haskell. Break-up of sea ice by ocean waves. *Annals Glaciol.*, 27:438–442, 1998.

R. Massom and S. Stammerjohn. Antarctic sea ice variability: Physical and ecological implications. *Polar Sci.*, 4:149–458, 2010.

M. H. Meylan. Wave response of an ice floe of arbitrary geometry. *J. Geophys. Res.*, 107:doi:10.1029/2000JC000713, 2002.

F. Montiel, L. G. Bennetts, V. A. Squire, F. Bonnefoy, and P. Ferrant. Hydroelastic response of floating elastic disks to regular waves. Part 2: Modal analysis. *J. Fluid Mech.*, 723:629–652, 2013a.

F. Montiel, F. Bonnefoy, P. Ferrant, L. G. Bennetts, V. A. Squire, and P. Marsault. Hydroelastic response of floating elastic disks to regular waves. Part 1: Wave tank experiments. *J. Fluid Mech.*, 723:604–628, 2013b.

J. N. Newman. Wave effects on a deformable body. *Appl. Ocean Res.*, 16:47–59, 1994.

S. J. Prinsenberg and I. K. Peterson. Observing regional-scale pack-ice decay processes with helicopter-borne sensors and moored upward-looking sonars. *Annals Glaciol.*, 52:35–42, 2011.

V. A. Squire. Of ocean waves and sea-ice revisited. *Cold Reg. Sci. Technol.*, 49:110–133, 2007.

V. A. Squire. Past, present and impendent hydroelastic challenges in the polar and subpolar seas. *Phil. Trans. R. Soc. Lond. A*, 369:2813–2831, 2011.

V. A. Squire, J. P. Dugan, P. Wadhams, P. J. Rottier, and A. K. Liu. Of ocean waves and sea ice. *Annu. Rev. Fluid Mech.*, 27:115–168, 1995.

M. Steele. Sea ice melting and floe geometry in a simple ice-ocean model. *J. Geophys. Res.*, 94((C9)): 17,729–17,738, 1992.

J. Thomson and W. E. Rogers. Swell and sea in the emerging Arctic Ocean. *Geophys. Res. Lett.*, 41: 3136–3140, 2014.

S. Timoshenko and S. Woinowsky-Krieger. *Theory of plates and shells.* McGraw-Hill, 2nd edition, 1959.

P. Wadhams, A. E. Gill, and P. F. Linden. Transects by submarine of the East Greenland Polar Front. *Deep Sea Res.*, 26(A):1311–1327, 1979.

T. D. Williams, L. G. Bennetts, D. Dumont, V. A. Squire, and L. Bertino. Wave-ice interactions in the marginal ice zone. Part 1: Theoretical foundations. *Ocean Model.*, 71:DOI: 10.1016/j.ocemod.2013.05.010, 2013a.

T. D. Williams, L. G. Bennetts, D. Dumont, V. A. Squire, and L. Bertino. Wave-ice interactions in the marginal ice zone. Part 2: Numerical implementation and sensitivity studies along 1d transects of the ocean surface. *Ocean Model.*, 71:DOI: 10.1016/j.ocemod.2013.05.011, 2013b.